npj | quantum materials www.nature.com/npjquantmats

ARTICLE OPEN

Check for updates

Interaction of in-plane Drude carrier with *c*-axis phonon in $PdCoO_2$

Dongmin Seo[1,2], Gihyeon Ahn[3], Gaurab Rimal[4], Seunghyun Khim[5], Suk Bum Chung[1,6,7], A. P. Mackenzie[5,8], Seongshik Oh[4], S. J. Moon[3]✉ and Eunjip Choi[1]✉

We performed polarized reflection and transmission measurements on the layered conducting oxide $PdCoO_2$ thin films. For the *ab*-plane, an optical peak near $\Omega \approx 750\ \mathrm{cm}^{-1}$ drives the scattering rate $1/\tau(\omega)$ and effective mass $m^*(\omega)$ of the Drude carrier to increase and decrease respectively for $\omega \geqq \Omega$. For the *c*-axis, a longitudinal optical phonon (LO) is present at Ω as evidenced by a peak in the loss function $\mathrm{Im}[-1/\varepsilon_c(\omega)]$. Further polarized measurements in different light propagation (**q**) and electric field (**E**) configurations indicate that the Peak at Ω results from an electron-phonon coupling of the *ab*-plane carrier with the *c*-LO phonon, which leads to the frequency-dependent $1/\tau(\omega)$ and $m^*(\omega)$. This unusual interaction was previously reported in high-temperature superconductors (HTSC) between a non-Drude, mid-infrared (IR) band and a *c*-LO. On the contrary, it is the Drude carrier that couples in $PdCoO_2$. The coupling between the *ab*-plane Drude carrier and *c*-LO suggests that the *c*-LO phonon may play a significant role in the characteristic *ab*-plane electronic properties of $PdCoO_2$, including the ultra-high dc-conductivity, phonon-drag, and hydrodynamic electron transport.

npj Quantum Materials (2023)8:74 ; https://doi.org/10.1038/s41535-023-00607-1

INTRODUCTION

The interaction of an electron with a phonon plays a key role in emergent phenomena such as the polaron, charge density wave, and superconductivity. The electron-phonon interaction manifests itself, among others, in the ac-response of the material, including optical reflectance and dielectric functions[1]. In HTSC, the *ab*-plane optical conductivity exhibits an electronic continuum at the mid-IR range. Interestingly, for most HTSC compounds such as $YBa_2Cu_3O_{7-\delta}$[2], $Bi_2Sr_2CaCu_2O_8$[3], and others[4,5], a particular type of spectral feature, i.e., narrow dips or minima appear on top of the broad mid-IR band at multiple photon energies. In 1992, Reedyk and Timusk discovered that the minima are associated with optical phonons propagating along the *c*-axis of the lattice, specifically, longitudinal optical phonons. The unusual activation of the *c*-axis phonons in the *ab*-plane reflectivity, normally forbidden due to the momentum selection rule, results from the coupling of the in-plane electron with the *c*-axis LO phonons[6]. This electron-phonon interaction has drawn attention from the perspective of possible superconductivity pairing mechanisms. On the other hand, there has been a question as to whether a similar kind of interaction occurs in other layered metallic oxides as well. To the best of our knowledge, such material has not yet been reported.

The delafossite $PdCoO_2$ consists of triangular Pd-planes that alternate with the CoO_6 planes and are stacked along the *c*-axis. The in-plane electrical conduction occurs predominantly in the Pd-sheet[7–16], giving rise to dc-conductivity $\sigma = 3.8 \times 10^5 \Omega^{-1}\mathrm{cm}^{-1}$ at room temperature[17], which is, remarkably, higher than noble metals such as Au or Ag[18]. The mean free path of electrons is as long as 20 μm at low temperatures, making this material a promising candidate for hydrodynamic and other non-local transport studies[19,20]. An optical study by Homes et al. suggested that, importantly, the *ab*-plane electrons may couple with *c*-axis LO phonons in $PdCoO_2$[21]. This claim was based on two phonon-like peaks that are expected to be silent in the *ab*-plane reflectivity yet appear in the actual measurements. This interesting suggestion, however, was not supported by compelling experimental evidence.

In this work, we directly address this issue by performing optical measurements using a distinct approach from ref. [21]: First, we probe both the *ab*-plane and the *c*-axis. For the *ab*-plane study, we employ a thin film, $PdCoO_2$, instead of a single crystal. The latter has an extremely high reflection in the infrared range, which, as mentioned in ref. [21], poses difficulty in carrying out a quantitative analysis. Such a problem can be largely alleviated by using a $PdCoO_2$ thin film for which reflectivity is significantly reduced. Additionally, a thin film allows for transmission measurements, which, when combined with the reflection, leads to precise optical dielectric functions. Second, for the *c*-axis study, we take advantage of a single crystal $PdCoO_2$ in combination with a focused beam of microscopic Fourier transform infrared (FTIR) spectroscopy, which makes the optical measurement possible despite the limited sample dimension along the *c*-axis. Through the complementary studies on a thin film (for the *ab*-plane) and a single crystal (for the *c*-axis), we firmly establish that the *ab*-plane electrons of $PdCoO_2$ couple with a longitudinal *c*-axis optical phonon. While the coupling in HTSC occurred between the (non-Drude) mid-infrared band and *c*-LO, it is the Drude carrier that couples in $PdCoO_2$.

[1]Department of Physics, University of Seoul, Seoul 02504, Republic of Korea. [2]Department of Smart Cities, University of Seoul, Seoul 02504, Republic of Korea. [3]Department of Physics, Hanyang University, Seoul 04763, Republic of Korea. [4]Department of Physics and Astronomy, Rutgers, The State University of New Jersey, Piscataway, New Jersey 08854, USA. [5]Max Planck Institute for Chemical Physics of Solids, Nöthnitzer Straße 40, 01187 Dresden, Germany. [6]Natural Science Research Institute, University of Seoul, Seoul 02504, Republic of Korea. [7]School of Physics, Korea Institute for Advanced Study, Seoul 02455, Republic of Korea. [8]Scottish Universities Physics Alliance, School of Physics and Astronomy, University of St Andrews, St Andrews KY16 9SS, United Kingdom. ✉email: soonjmoon@hanyang.ac.kr; echoi@uos.ac.kr

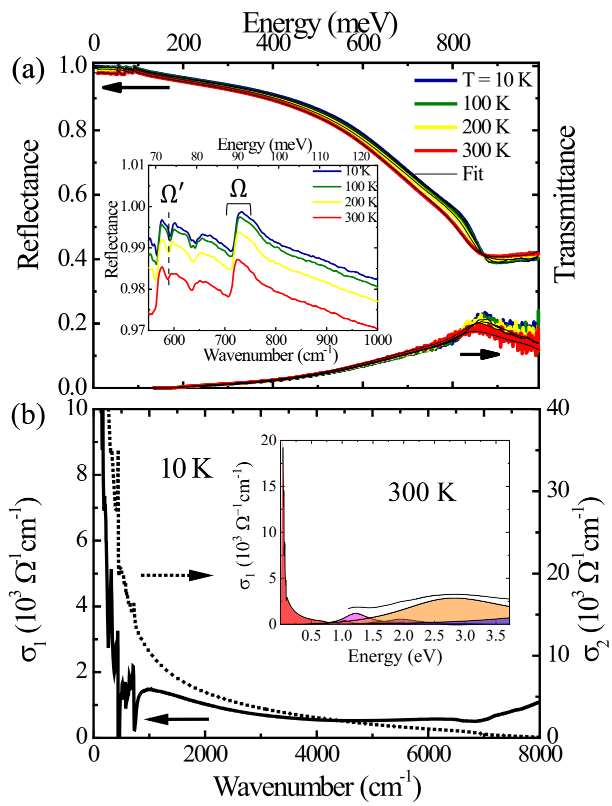

Fig. 1 **Reflectance, transmittance, and optical conductivity of $PdCoO_2$.** **a** Reflectance and transmittance of a $PdCoO_2$ thin film (thickness = 90 nm). The inset highlights that there is a peak around ~90 meV. **b** Real and imaginary parts of the optical conductivity. Inset depicts the wide-range $\sigma_1(\omega)$ up to 4 eV, which consists of Drude component (red) and multiple interband transition peaks (colored).

RESULTS

Extended Drude analysis

Figure 1a shows the reflectance $R(\omega)$ and transmittance $T(\omega)$ of the $PdCoO_2$ thin film for $\hbar\omega < 0.1$ eV. We fit $R(\omega)$ and $T(\omega)$ simultaneously using the multilayer (film+substrate) analysis algorithm of the Kramers-Kronig (KK) constrained RefFit program[22]. The dielectric functions of the bare Al_2O_3-substrate were characterized separately and fed into the analysis. Figure 1b displays $\sigma_1(\omega)$ and $\sigma_2(\omega)$, the real and imaginary optical conductivity of $PdCoO_2$, respectively, obtained from the fit at $T = 10$ K. They consist of an intra-band (Drude) response in the low-energy range and interband transitions at high energy $\hbar\omega > 0.8$ eV. As $PdCoO_2$ possesses only one conduction band as evidenced by experiments and theory[9–11,13,17,23,24], the Drude conductivity represents the response of the single-band electron. When compared to the previous optical study on a single crystal $PdCoO_2$[21], the interband transitions of our film are almost identical, whereas the Drude peak is notably broader. The latter is attributed to additional scatterings of the carrier at the twin boundary and the top / bottom surfaces of the film[25]. In the inset of Fig. 1a, we highlight that there is a distinct peak-like feature at $\hbar\omega = 90$ meV in $R(\omega)$. We label it conveniently as Peak-Ω and will revisit it frequently later for data analysis. To add, Ω′ refers to a dip at a lower energy.

In Fig. 2, we show the scattering rate $1/\tau(\omega)$ and effective mass $m^*(\omega)$ of the Drude carrier. They are calculated from the Drude

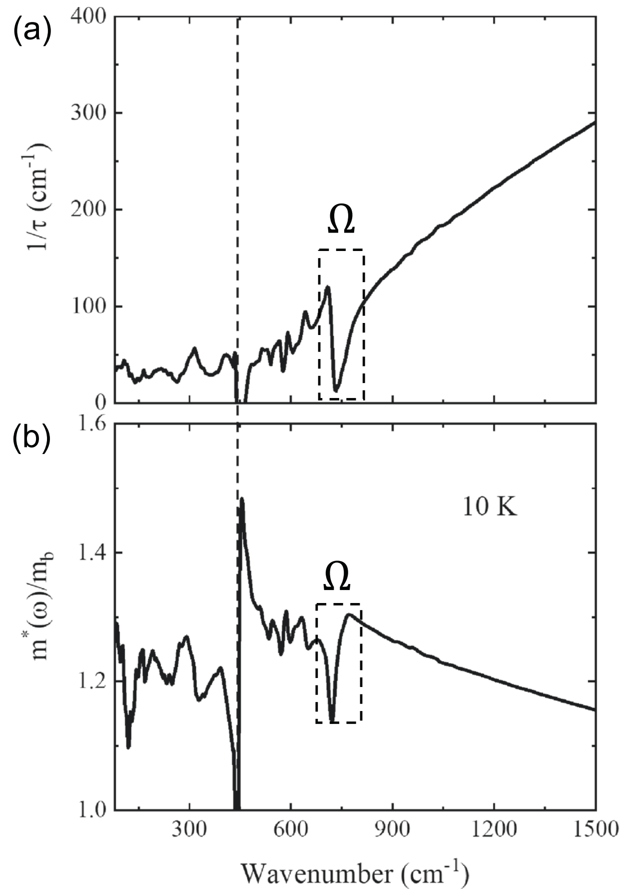

Fig. 2 **Extended Drude analysis results.** **a** Frequency-dependent scattering rate $1/\tau(\omega)$ and **b** mass enhancement $m^*(\omega)/m_b$. They are calculated from the Drude conductivity through Eqs. (1) and (2), where ω_p (= 28500 cm^{-1}) was determined from $\omega_p^2/8 = \int_0^{\omega_c} \sigma_{Drude}(\omega')d\omega'$ with $\sigma_{Drude}(\omega) = \sigma(\omega)$-$\sigma_{Interband}(\omega)$ and the cutoff frequency $\omega_c = 15000$ cm^{-1}. The notation Ω corresponds to the optical feature in the reflectivity, Peak-Ω in Fig. 1a. The spurious noise at $\omega = 450$ cm^{-1} (dashed line) is caused by the substrate. (See Supplementary Fig. 2).

$\sigma_1(\omega)$ and $\sigma_2(\omega)$ using the extended Drude analysis formula.

$$\frac{1}{\tau(\omega)} = \frac{\omega_p^2}{4\pi} \frac{\sigma_1(\omega)}{\sigma_1^2(\omega) + \sigma_2^2(\omega)} \quad (1)$$

$$\frac{m^*(\omega)}{m_b} = \frac{\omega_p^2}{4\pi} \frac{\sigma_2(\omega)}{\sigma_1^2(\omega) + \sigma_2^2(\omega)} \frac{1}{\omega} \quad (2)$$

The $1/\tau(\omega)$ increases markedly for $\omega > \Omega$ and $m^*(\omega)$ drops from the same frequency. At $\hbar\omega = 90$ meV, there is a dispersive structure in $1/\tau(\omega)$ and $m^*(\omega)$ that triggers the frequency-dependent changes. This structure originates from the Peak-Ω in $R(\omega)$. The frequency-dependent $1/\tau(\omega)$ and $m^*(\omega)$ are the characteristic behavior of an electron-boson interaction: For a conducting material with an electron-boson interaction, $1/\tau(\omega)$ increases as ω exceeds the boson energy, and simultaneously, $m^*(\omega)/m_b$ begins to decrease from a dressed mass (>1) to bare band mass (=1)[26–31]. Figure 2 shows that an electron-boson coupling is occurring in $PdCoO_2$ with a boson mode located at $\omega = \Omega$.

To ensure that the frequency-dependent $1/\tau(\omega)$ and $m^*(\omega)$ are intrinsic properties of $PdCoO_2$, we synthesized a pure Pd-thin film (thickness = 15 nm) using molecular beam epitaxy (MBE) on the same substrate (Al_2O_3) and performed the same optical measurements (R and T) and extended Drude analysis. The Pd-film is classified as a noble metal such as Au or Ag films. In contrast to $PdCoO_2$, $1/\tau(\omega)$ and $m^*(\omega)$ of the Pd-film are independent of frequency as expected for a simple Drude metal. (See Supplementary Fig. 1) This comparative study supports that $1/\tau(\omega)$ and $m^*(\omega)$ in Fig. 2 are not artifacts caused by, for example, the Al_2O_3 substrate but are the genuine properties of $PdCoO_2$. In addition, the Pd-film does not show Peak-Ω (and Ω′) in R(ω), indicating that Peak-Ω (and Ω′) is intrinsic to $PdCoO_2$ as well. (See Supplementary Fig. 2). In Fig. 2, $1/\tau(\omega)$ and $m^*(\omega)$ become considerably noisy for the range $\omega < \Omega$. The unwanted noises are caused mostly by the strong optical phonons of Al_2O_3, which we present in detail in Supplementary Fig. 2. Ideally, the substrate phonons should be isolated from the thin film during the data analysis (fitting). However, in practice, they are not perfectly removed, causing the noise. Importantly, Supplementary Fig. 2 demonstrates that, unambiguously, Peak-Ω arises not from the substrate but from $PdCoO_2$. Given that Peak-Ω is driving the frequency-dependent $1/\tau(\omega)$ and $m^*(\omega)$, it is crucial to unveil the origin of Peak-Ω in order to understand the electron-boson interaction of $PdCoO_2$.

Polarization-dependent measurements and origin of Peak-Ω

In Fig. 3a, we measured the *c*-axis reflectance $R_c(\omega)$ of the $PdCoO_2$ single crystal. To measure $R_c(\omega)$, a focused IR beam from a microscopic FTIR polarized along the *c*-axis (**E** ||*c*) was illuminated on the side facet of the d ~ 100 μm-thick single crystal. In this manner, reproducible data were obtained for $\omega > \sim 500$ cm^{-1}. The $R_c(\omega)$ shows a prominent structure at $\hbar\omega = 90$ meV and a minor one at 70 meV. The wide-range $R_c(\omega)$ (inset) reveals an insulating

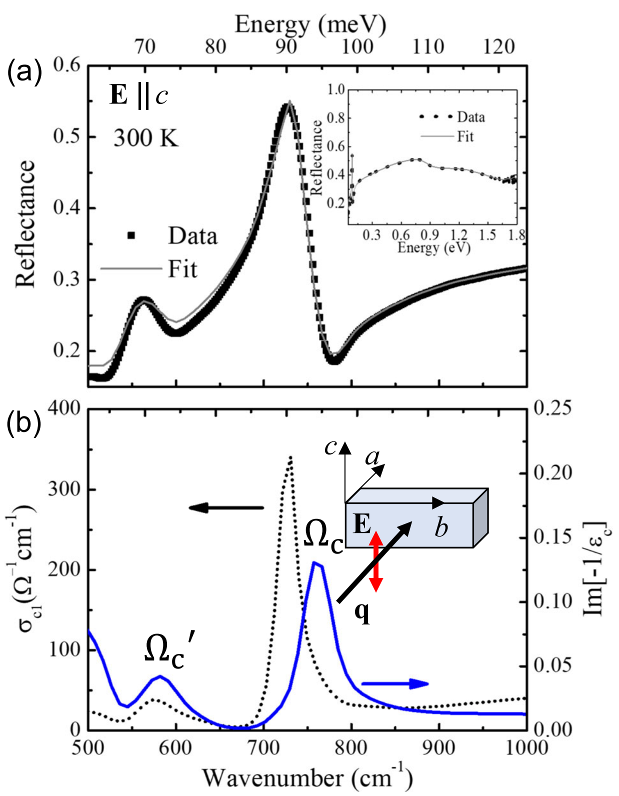

Fig. 3 Optical conductivity and dielectric loss function of the *c*-axis. a Reflectance $R_c(\omega)$ measured with the light polarized as **E** ||*c* on the $PdCoO_2$ single crystal. Inset shows the wide-range $R_c(\omega)$ up to 1.8 eV. **b** The *c*-axis optical conductivity and dielectric loss function. Inset shows that the light propagates along the *ab*-plane, **q** ||*ab*, and E-field is polarized along the *c*-axis, **E** ||*c*. Here Ω_c and Ω_c' denote the two peaks of the $\mathrm{Im}[-1/\varepsilon_c(\omega)]$.

behavior of the *c*-axis, which contrasts sharply with the metallic R(ω) of the *ab*-plane. We fit the $R_c(\omega)$ using the KK-constrained RefFit and calculated the complex *c*-axis optical conductivity $\sigma_c(\omega)$ and dielectric constant $\varepsilon_c(\omega)$. In the fit, we constrained $\sigma_c(\omega)$ to match the *c*-axis dc-conductivity at $\omega = 0$[32]. In Fig. 3b, we show the real part of $\sigma_c(\omega)$. $\sigma_{c1}(\omega)$ is peaked at $\hbar\omega = 730$ cm^{-1} and 570 cm^{-1}, which represents two transverse optical phonons (TO) of the *c*-axis. These *c*-TO phonons propagate along the *ab*-plane, **q** ||*ab*. We also calculate the dielectric loss function $\mathrm{Im}[-1/\varepsilon_c(\omega)]$, which shows two peaks Ω_c and Ω_c' representing the *c*-axis LO phonons. They propagate along **q** ||*c*. Note that, remarkably, Ω_c is very close to Peak-Ω, suggesting that it is a possible source of Peak-Ω. The *c*-TO phonon (**q** ||*ab*), which is also close to Peak-Ω, is not excited in the normal-incidence thin film measurements (**q** ||*c*) in Fig. 1, thus cannot create Peak-Ω. As for Ω_c', its energy is close to the dip Ω′ of Fig. 1.

To confirm the presumption that Peak-Ω originates from Ω_c, we perform further polarized reflectance measurements. In Fig. 4a, incident light propagates along the *c*-axis while the electric field is parallel to the *ab*-plane. This optical configuration (**q** ||*c*, **E** ||*ab*) can activate the *ab*-plane TO and the *c*-axis LO phonon. In Fig. 4b, we employed a different optical configuration **q** ||*a* and **E** ||*b*, which activates the *b*-TO but not the *c*-LO. (To note, we use '*a*' and '*b*' to represent two orthogonal axes of the *ab*-plane but they do not indicate any specific crystallographic directions. The terms *a*-TO and *b*-TO are equivalent to *ab*-TO.) The R(ω) in Fig. 4d, e show that Peak-Ω is activated in Fig. 4a but is absent in Fig. 4b, demonstrating that *ab*-TO is excluded from the source of Peak-Ω, thus leaving the *c*-LO (Ω_c) the only remaining candidate. The *ab*-TO phonons are another possible source of Peak-Ω but, according to ref. [21], they are far from Peak-Ω. In general, a *c*-axis optical phonon of a layered material does not appear in the *ab*-plane reflectivity due to forbidden symmetry. In $PdCoO_2$, however, Ω_c manifests itself in the *ab*-plane reflectivity as a result of coupling with the *ab*-plane Drude carrier. This coupling leads to the frequency-dependent $1/\tau(\omega)$ and $m^*(\omega)$ of Fig. 2.

In our near-normal ($\theta = 10°$) reflectance measurement, incident light contains a small **E** ||*c* component, which may cause the *c*-axis phonons to leak into the *ab*-plane reflectivity. In this case, Peak-Ω may appear in R(ω) even if the electron-phonon coupling was absent. To test if this is the case for Fig. 4d, we measured R(ω) using the s- and p-polarization as shown in Fig. 4c: In the s-polarization, the light has no **E** ||*c* component, whereas the p-polarization does have a finite **E** ||*c* component. The R(ω) in Fig. 4f shows that Peak-Ω is activated in the s-polarization with similar strength as in the p-polarization. This result rules out the leakage scenario of Peak-Ω. To reinforce our conclusion, we theoretically calculated the grazing-incidence R(ω) at incidence angles $\theta = 10°$ and 20°. For this, we used the *ab*-plane and *c*-axis dielectric functions measured in Figs. 1 and 3, respectively. The calculation results, shown in Supplementary Fig. 3, reveal that at $\theta = 20°$, the *c*-LO leaks into the *ab*-plane reflectivity in the p-polarization, giving rise to a peak with 5×10^{-4} in height. However, this peak height is far weaker than the actual height of Peak-Ω in Fig. 4f, 0.01. Furthermore, at the experimental angle $\theta = 10°$, the calculated leakage becomes even smaller, and the peak is too weak to be detected. This observation supports again that the E-field leakage cannot account for Peak-Ω in R(ω). We thus conclude that the *c*-LO does couple with the *ab*-plane Drude carrier manifesting itself as Peak-Ω in the *ab*-plane reflectance.

Fano analysis of the *ab*-plane and the *c*-axis

We performed the Fano fit of the *ab*-plane optical conductivity employing the Fano expression[33],

$$\sigma_F(\omega) = i\sigma_0 \frac{(q-i)^2}{i+\epsilon} \tag{3}$$

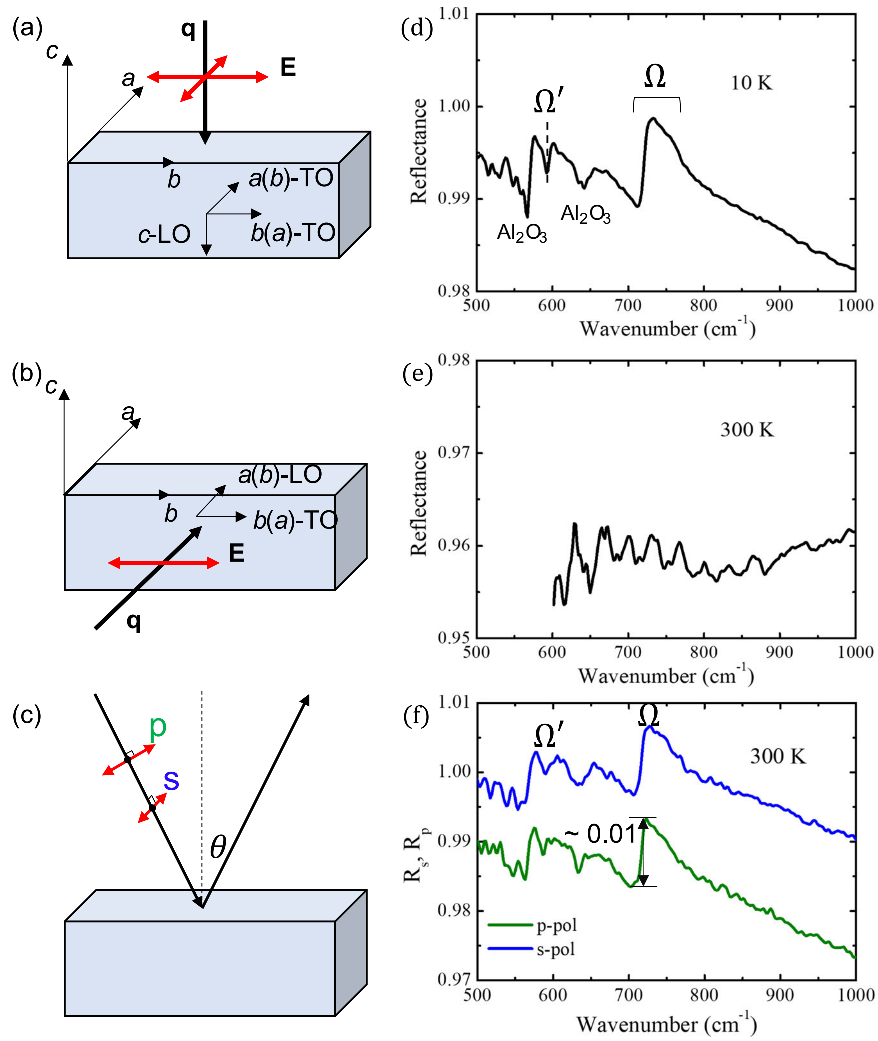

Fig. 4 Polarization-dependent reflectance of $PdCoO_2$. Polarization-dependent reflectance of $PdCoO_2$. **a** Light propagates along **q** $\|c$ and **E**-field is unpolarized. **b** Light propagates along **q** $\|a(b)$ and **E**-field is polarized along **E** $\|b(a)$. **c** s- and p-polarized lights are incident at an incidence angle $\theta = 10°$. The reflectance data of (**a–c**) are shown in (**d–f**), respectively. The thin film was used for (**a**) and (**c**), and the single crystal was used for (**b**).

where $\epsilon = (\omega^2 - \omega_0^2)/\gamma\omega$, σ_0, ω_0, γ and q are the strength, frequency, width, and asymmetry of the phonon, respectively. In Eq. (3), the Fano asymmetry increases as $|q|$ becomes smaller[33–35]. For the *ab*-plane, Fano fit to the Peak-Ω is shown in Fig. 5b. The fit yields $q = -1$. Here the fit is good at $\omega > 715$ cm^{-1} but becomes poor $\omega < 715$ cm^{-1} due to the strong phonon peaks of the substrate. The two symbols * in Fig. 5 indicate the positions of the substrate optical phonons (Supplementary Fig. 5), which coincide with the deviations from the fit. The *c*-axis LO phonon emerges as a peak in the loss function $\mathrm{Im}[-1/\varepsilon_c]$, as we showed in Fig. 3b and explained in the main text. We fit $\mathrm{Im}[-1/\varepsilon_c]$ using $\varepsilon(\omega) = \varepsilon_\infty + \frac{4\pi i}{\omega}\sigma(\omega)$ and Eq. (3). Fitting result shows $q = 8$ as shown in Fig. 5b. This q is larger than the $|q| = 1$ of the Peak-Ω of the *ab*-plane, indicating that the electron-phonon interaction is weaker in the *c*-axis than in the *ab*-plane. To look for the origin of this result, we note that the electron-phonon coupling strength is determined from

$$\alpha^2F(\omega) = N(0)\frac{\sum_{\mathbf{k},\mathbf{k}'} w(\mathbf{k},\mathbf{k}')|M_{\mathbf{k},\mathbf{k}'}|^2\delta(\hbar\omega - \hbar\omega_{\mathbf{k}-\mathbf{k}'})\delta(\xi_\mathbf{k})\delta(\xi_{\mathbf{k}'})}{\sum_{\mathbf{k},\mathbf{k}'} w(\mathbf{k},\mathbf{k}')\delta(\xi_\mathbf{k})\delta(\xi_{\mathbf{k}'})} \tag{4}$$

where $M_{\mathbf{k},\mathbf{k}'}$ is the electron-phonon matrix element, $N(0)$ the density of states at the Fermi level, $w(\mathbf{k},\mathbf{k}') = (v_{\mathbf{k},i} - v_{\mathbf{k}',i})^2$ (i referring to the i-th component) is the electron velocity weighting factor[36,37]. Given that $PdCoO_2$ possesses the cylindrical Fermi surface that is open in the *c*-axis direction[11], the coupling strength can be different for the *ab*-plane and the *c*-axis. When the frequency is close to the *c*-axis LO mode energy minimum, k_z of the Drude carrier changes very little upon scattering due to the purely *c*-axis phonon dispersion. That this leads to the anisotropic electron-phonon coupling strength can be most easily shown for the simplified case of cylindrical Fermi surface[38], where $v_x = v_F\cos\phi$, $v_y = v_F\sin\phi$, and $v_z = v_\parallel \sin k_z$ with v_F and $v_\parallel$ independent of k_z. If the *c*-axis LO dispersion is approximated as $(\hbar\omega_\mathbf{q})^2 = E_1^2(1-\cos q_z) + E_0^2$ near its minimum energy E_0 (=90 meV in our measurement), we have the inequality relation

$$\begin{aligned} \alpha_\perp^2F(\omega) &= N(0)|M|^2\frac{\hbar\omega}{2\pi\sqrt{(\hbar^2\omega^2-E_0^2)(4E_1^2+E_0^2-\hbar^2\omega^2)}} \\ >\alpha_\parallel^2F(\omega) &= N(0)|M|^2\frac{\hbar\omega}{4\pi E_1^2}\sqrt{\frac{\hbar^2\omega^2-E_0^2}{4E_1^2+E_0^2-\hbar^2\omega^2}}, \end{aligned} \tag{5}$$

where '⊥' refers to the components perpendicular to the *c*-axis, i.e., the *ab*-plane, '∥' to the component parallel to the *c*-axis. Here $M_{\mathbf{k},\mathbf{k}'}$ is taken to be constant due to a strongly screened electron-phonon interaction of $PdCoO_2$. This theoretical consideration

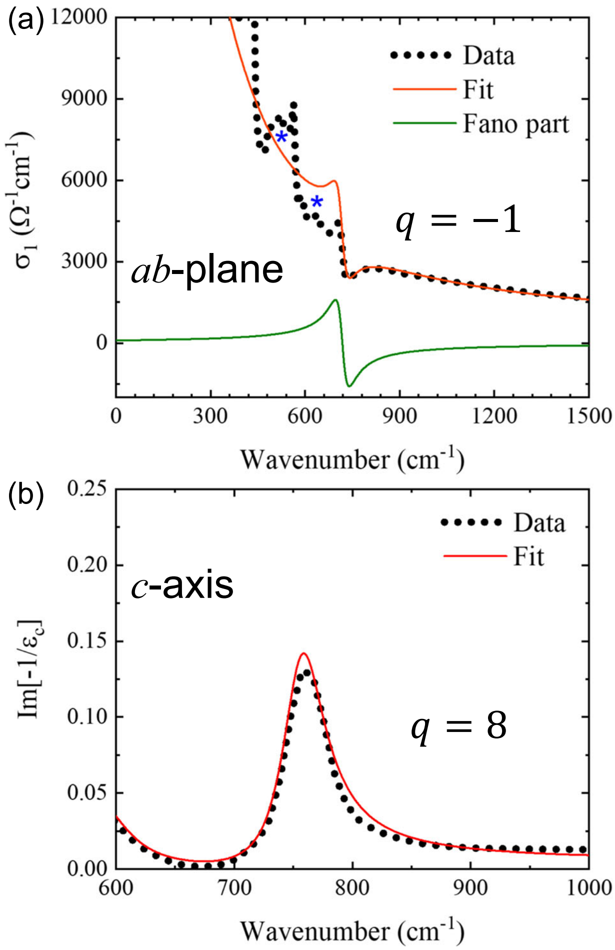

Fig. 5 Fano asymmetry analysis. Fano fit to **a** the optical conductivity data of *ab*-plane and **b** loss function of the *c*-axis at 300 K. Fano asymmetric parameters are $q = -1$ for the *ab*-plane and $q = 8$ for the *c*-axis. The two symbols * in Fig. 5 indicate the positions of the substrate optical phonons, which coincide with the deviations from the fit. The green curve in (**a**) shows the Fano asymmetric optical phonon.

supports the larger asymmetry (smaller *q*) of the *c*-LO phonon in the *ab*-plane than in the *c*-axis in Fig. 5.

DISCUSSION

To compare $PdCoO_2$ with HTSC, they are the two types of rare materials that exhibit the coupling of the *ab*-plane carrier with *c*-LO phonons. One major difference, however, is that the Drude carrier couples in $PdCoO_2$, whereas it is the mid-IR band in HTSC[6]. Therefore, in the latter, *c*-LO does not influence the dc-transport. On the contrary, the *c*-LO of $PdCoO_2$ may play a significant role in the *ab*-plane transport, such as the hydrodynamic charge flow. We emphasize that $PdCoO_2$ is the first layered material in which the *c*-LO couples with the *ab*-plane Drude carriers.

To discuss Ω', we examine if it arises from Ω_c' like Ω did from Ω_c. For this, we compare the *ab*-plane $\sigma_1(\omega)$ with the *c*-axis Im[$-1/\varepsilon_c(\omega)$] in Supplementary Fig. 4 following a similar approach as in ref. [6]. The Peak-Ω' occurs at the same energy as Ω_c' but with a significantly narrower width. On the contrary, for the single crystal $PdCoO_2$, an optical peak occurs in the *ab*-plane at the same energy and with similar width as Ω_c', supporting that the electron-phonon interaction persists for Ω'[21]. In the thin film, $\sigma_1(\omega)$ is highly uncertain in the region of Ω', hindering precise determination of the spectral shape. To definitely establish the correlation with Ω_c', improved measurements that overcome the noise are needed. To further compare the thin film and single crystal results, we note that Peak-Ω has an asymmetric, Fano-like shape in $\sigma_1(\omega)$ in both cases. However, they have the opposite Fano-asymmetry signs and different strengths of asymmetry (See Supplementary Fig. 4 and ref. [21]). Such differences suggest that substantial thickness-dependent effects exist for the electron-phonon coupling. Lastly, while we focused primarily on electron-phonon coupling in this paper, our data may suggest that another type of interaction, such as the electron-electron interaction, may apply to $PdCoO_2$ as well (See Supplementary Fig. 5).

In conclusion, we performed polarized infrared transmission and reflection measurements on a $PdCoO_2$ thin film. In the *ab*-plane, the scattering rate $1/\tau(\omega)$ and effective mass $m^*(\omega)$ of the Drude carriers increased and decreased for $\omega > \Omega$, respectively, driven by Peak-Ω. In the *c*-axis measurement on a single crystal, a longitudinal optical phonon was found at Ω_c as evidenced by a peak of the loss function Im[$-1/\varepsilon_c(\omega)$]. Further optical measurements employing different (**q, E**) configurations revealed that Peak-Ω is activated due to the interaction of the *ab*-plane Drude carriers with the *c*-LO phonon. This electron-phonon interaction leads to the frequency-dependent $1/\tau(\omega)$ and $m^*(\omega)$. Our conclusion was established through the extensive supporting measurements on the pure Pd-film, bare Al_2O_3 substrate, and the s- and p-polarized grazing-incidence reflection calculations. The coupling of the *ab*-plane Drude electron with the *c*-LO phonon implies that *c*-LO may play a significant role in the characteristic *ab*-plane carrier dynamics of $PdCoO_2$, such as the ultra-high dc-conductivity, phonon-drag, and hydrodynamic charge flow, which is worthy for further studies.

METHODS

Sample growth and characterizations

Epitaxial $PdCoO_2$ thin films (thickness = 90 nm) were grown on an Al_2O_3 substrate using the molecular beam epitaxy (MBE) technique and were characterized through various methods such as X-ray diffraction (XRD), reflection high energy electron diffraction (RHEED), transmission electron microscopy (TEM), etc.[25]. A 100 μm-thick high-quality single crystal was grown using the flux method and thoroughly characterized[39,40].

Optical measurements

The *ab*-plane optical transmittance and reflectance in the infrared range were measured on the thin film samples ($PdCoO_2$ + substrate) and the bare Al_2O_3 substrate using FTIR (Bruker Vertex 70v). The transmission and reflection power spectra were normalized by the blank and gold (Au), respectively, where the latter Au reference was coated on the sample using the in situ evaporation technique[41]. The results of these measurements are presented in Supplementary Fig. 7. A Spectroscopic Ellipsometer (J.A. Woollam VASE) was used to obtain the optical dielectric functions from 0.7 eV to 4 eV. The optical reflection of the *c*-axis was measured on a single crystal in combination with microscopic FTIR (Hyperion 2000). The a and b directions refer to a set of two orthogonal directions in the hexagonal plane, which is not aligned with respect to the crystal structure. For the *c*-axis reflectivity measurements, we carefully polished the side facet of the single crystal and then confirmed the surface quality by performing polarized reflectivity measurements, as presented in Supplementary Fig. 7.

DATA AVAILABILITY

The data that support the findings of this study are available in OSF with the identifier https://doi.org/10.17605/OSF.IO/B5RWV[42].

Received: 14 June 2023; Accepted: 23 November 2023;
Published online: 16 December 2023

REFERENCES

1. Basov, D. N., Averitt, R. D., Van Der Marel, D., Dressel, M. & Haule, K. Electrodynamics of correlated electron materials. *Rev. Mod. Phys.* **83**, 471 (2011).
2. Kamarás, K. et al. In a clean high-T_c superconductor you do not see the gap. *Phys. Rev. Lett.* **64**, 84–87 (1990).
3. Reedyk, M. et al. Far-infrared optical properties of $Bi_2Sr_2CaCu_2O_8$. *Phys. Rev. B* **38**, 11981–11984 (1988).
4. Reedyk, M., Timusk, T., Xue, J. & Greedan, J. Optical investigation of the metal-insulator transition in the Ca-free $Pb_2Sr_2LCu_3O_8$ (L = Y, Dy, Eu, Sm, Nd, and Pr) series. *Phys. Rev. B* **45**, 7406 (1992).
5. Foster, C. et al. Infrared reflection of epitaxial $Tl_2Ba_2CaCu_2O_8$ thin films in the normal and superconducting states. *Solid State Commun.* **76**, 651–654 (1990).
6. Reedyk, M. & Timusk, T. Evidence for a-b-plane coupling to longitudinal c-axis phonons in high-T_c superconductors. *Phys. Rev. Lett.* **69**, 2705–2708 (1992).
7. Higuchi, T. et al. Photoemission study on $PdCoO_2$. *J. Electron Spectrosc. Relat. Phenom.* **92**, 71–75 (1998).
8. Seshadri, R., Felser, C., Thieme, K. & Tremel, W. Metal-metal bonding and metallic behavior in some ABO_2 delafossites. *Chem. Mater.* **10**, 2189–2196 (1998).
9. Hasegawa, M. et al. Electronic structure of delafossite-type metallic oxide $PdCoO_2$. *Mater. Trans.* **42**, 961–964 (2001).
10. Eyert, V., Frésard, R. & Maignan, A. On the metallic conductivity of the delafossites $PdCoO_2$ and $PtCoO_2$. *Chem. Mater.* **20**, 2370–2373 (2008).
11. Noh, H.-J. et al. Anisotropic electric conductivity of delafossite $PdCoO_2$ studied by angle-resolved photoemission spectroscopy. *Phys. Rev. Lett.* **102**, 256404 (2009).
12. Noh, H.-J. et al. Orbital character of the conduction band of delafossite $PdCoO_2$ studied by polarization-dependent soft X-ray absorption spectroscopy. *Phys. Rev. B* **80**, 073104 (2009).
13. Ong, K. P., Zhang, J., John, S. T. & Wu, P. Origin of anisotropy and metallic behavior in delafossite $PdCoO_2$. *Phys. Rev. B* **81**, 115120 (2010).
14. Mackenzie, A. P. The properties of ultrapure delafossite metals. *Rep. Prog. Phys.* **80**, 032501 (2017).
15. Daou, R., Frésard, R., Eyert, V., Hébert, S. & Maignan, A. Unconventional aspects of electronic transport in delafossite oxides. *Sci. Technol. Adv. Mater.* **18**, 919–938 (2017).
16. Harada, T. Thin-film growth and application prospects of metallic delafossites. *Mater. Today Adv.* **11**, 100146 (2021).
17. Hicks, C. W. et al. Quantum oscillations and high carrier mobility in the delafossite $PdCoO_2$. *Phys. Rev. Lett.* **109**, 116401 (2012).
18. Lynch, D. W. & Hunter, W. Comments on the optical constants of metals and an introduction to the data for several metals. *Handbook of Optical Constants of Solids*, 275–367 (Elsevier, 1997).
19. Moll, P. J., Kushwaha, P., Nandi, N., Schmidt, B. & Mackenzie, A. P. Evidence for hydrodynamic electron flow in $PdCoO_2$. *Science* **351**, 1061–1064 (2016).
20. Nandi, N. et al. Unconventional magneto-transport in ultrapure $PdCoO_2$ and $PtCoO_2$. *NPJ Quant. Mater.* **3**, 66 (2018).
21. Homes, C., Khim, S. & Mackenzie, A. P. Perfect separation of intraband and interband excitations in $PdCoO_2$. *Phys. Rev. B* **99**, 195127 (2019).
22. Kuzmenko, A. Kramers–Kronig constrained variational analysis of optical spectra. *Rev. Sci. Instrum.* **76**, 083108 (2005).
23. Kim, K., Choi, H. C. & Min, B. Fermi surface and surface electronic structure of delafossite $PdCoO_2$. *Phys. Rev. B* **80**, 035116 (2009).
24. Ong, K. P., Singh, D. J. & Wu, P. Unusual transport and strongly anisotropic thermopower in $PtCoO_2$ and $PdCoO_2$. *Phys. Rev. Lett.* **104**, 176601 (2010).
25. Brahlek, M. et al. Growth of metallic delafossite $PdCoO_2$ by molecular beam epitaxy. *Phys. Rev. Mater.* **3**, 093401 (2019).
26. Carbotte, J. Properties of boson-exchange superconductors. *Rev. Mod. Phys.* **62**, 1027 (1990).
27. Allen, P. Electron-phonon effects in the infrared properties of metals. *Phys. Rev. B* **3**, 305 (1971).
28. Shulga, S., Dolgov, O. & Maksimov, E. Electronic states and optical spectra of HTSC with electron-phonon coupling. *Phys. C Supercond.* **178**, 266–274 (1991).
29. Stricker, D. et al. Optical response of Sr_2RuO_4 reveals universal fermi-liquid scaling and quasiparticles beyond Landau theory. *Phys. Rev. Lett.* **113**, 087404 (2014).
30. Kostic, P. et al. Non-fermi-liquid behavior of $SrRuO_3$: evidence from infrared conductivity. *Phys. Rev. Lett.* **81**, 2498 (1998).
31. Schlesinger, Z. et al. Superconducting energy gap and normal-state conductivity of a single-domain $YBa_2Cu_3O_7$ crystal. *Phys. Rev. Lett.* **65**, 801 (1990).
32. Putzke, C. et al. h/e oscillations in interlayer transport of delafossites. *Science* **368**, 1234–1238 (2020).
33. Damascelli, A., Schulte, K., Van der Marel, D. & Menovsky, A. Infrared spectroscopic study of phonons coupled to charge excitations in FeSi. *Phys. Rev. B* **55**, R4863 (1997).
34. Fano, U. Effects of configuration interaction on intensities and phase shifts. *Phys. Rev.* **124**, 1866 (1961).
35. Uykur, E., Ortiz, B. R., Wilson, S. D., Dressel, M. & Tsirlin, A. A. Optical detection of the density-wave instability in the kagome metal KV_3Sb_5. *NPJ Quant. Mater.* **7**, 16 (2022).
36. Allen, P. B. & Schulz, W. W. Bloch-Boltzmann analysis of electrical transport in intermetallic compounds: ReO_3, $BaPbO_3$, $CoSi_2$, and Pd_2Si. *Phys. Rev. B* **47**, 14434 (1993).
37. Poole, C. K., Farach, H. A. & Creswick, R. J. *Handbook of Superconductivity* (Elsevier, 1999).
38. Bachmann, M. D. et al. Super-geometric electron focusing on the hexagonal fermi surface of $PdCoO_2$. *Nat. Commun.* **10**, 5081 (2019).
39. Shannon, R. D., Rogers, D. B. & Prewitt, C. T. Chemistry of noble metal oxides. I. Syntheses and properties of ABO_2 delafossite compounds. *Inorg. Chem.* **10**, 713–718 (1971).
40. Takatsu, H., Yonezawa, S., Fujimoto, S. & Maeno, Y. Unconventional anomalous Hall effect in the metallic triangular-lattice magnet $PdCrO_2$. *Phys. Rev. Lett.* **105**, 137201 (2010).
41. Homes, C. C., Reedyk, M., Cradles, D. & Timusk, T. Technique for measuring the reflectance of irregular, submillimeter-sized samples. *Appl. Opt.* **32**, 2976–2983 (1993).
42. Seo, D. Interaction of in-plane Drude carrier with c-axis phonon in $PdCoO_2$. OSF https://osf.io/b5rwv/ (2023).

ACKNOWLEDGEMENTS

We thank C.C. Homes, D. Valentinis, J. Zaannen, D. Van Der Marel, Hyoung Joon Choi, and Han-Jin Noh for their helpful discussions. E.C. was supported by the NRF-2021R1A2C1009073 of Korea funded by the Ministry of Education. D.S. was partially supported by MOLIT as an Innovative Talent Education Program for Smart City. The work at Rutgers University is supported by the National Science Foundation's DMR2004125 and the Army Research Office's W911NF2010108. S.B.C. was supported by the National Research Foundation of Korea (NRF) grants funded by the Korean government (MSIT)(NRF-2023R1A2C1006144, NRF-2020R1A2C1007554, and NRF-2018R1A6A1A06024977). Research in Dresden benefits from the environment provided by the DFG Cluster of Excellence ct.qmat (EXC 2147, project ID 390858490). The work at HYU was supported by the NRF grant funded by the Korean government (MSIT) (2022R1F1A1072865), the BrainLink program funded by MSIT (2022H1D3A3A01077468), and the Quantum Simulator Development Project for Materials Innovation through the NRF funded by MSIT (2023M3K5A1094813).

AUTHOR CONTRIBUTIONS

E.C. conceived the project. G.R. and S.O. synthesized and characterized thin film samples. S.K. and A.P.M. synthesized and characterized single-crystal samples. D.S. and G.A. performed the optical measurements and analysis. E.C. and S.M. supervised the optical measurement. S.B.C. performed the theoretical analysis. D.S., S.B.C., S.M., and E.C. wrote the manuscript with contributions from all authors.

COMPETING INTERESTS

The authors declare no competing interests.

ADDITIONAL INFORMATION

Supplementary information The online version contains supplementary material available at https://doi.org/10.1038/s41535-023-00607-1.

Correspondence and requests for materials should be addressed to S. J. Moon or Eunjip Choi.